Conference or Workshop Item:
Arabi, Sadaf, Koshuriyan, Zamir and Sescu, Adrian (2024) Investigation of Orthogonal Modes in High-speed Axisymmetric Jet Turbulence: Instantaneous vs. Statistical Data. In: Twenty-first International Conference on Flow Dynamics, November 18 - 20, 2024, Sendai International Center, Sendai, Miyagi, Japan., 18-20 Nov 2024.

Investigation of Orthogonal Modes in High-speed Axisymmetric Jet Turbulence: Instantaneous vs. Statistical Data

Sadaf Arabi[1], M. Z. A. Koshuriyan[1], Adrian Sescu[2]

[1] Department of Mathematics, University of York
Heslington, York YO10 5DD, United Kingdom

[2] Mississippi State University
Starkville, MS 39762, USA

ABSTRACT

We investigate orthogonal turbulence modes in a high-speed axisymmetric jet via the S-POD algorithm. We use S-POD as a barometer to gauge the energy content of the turbulence measured by its statistics vs. instantaneous flow data. Our results show that the statistics possesses modes with uniform energy distribution at low frequencies bounded by a ratio of modal energies much greater than unity, indicating that most of the auto-covariance energy is contained within a short temporal neighborhood about its auto-correlation amplitude.

1. Introduction

Data-driven flow techniques are utilized nowadays to provide insights into the coherent features of turbulence. In these methods, an empirical mode basis is constructed to capture dominant flow structures. Comprehensive reviews of different forms of Proper Orthogonal Decomposition (POD) techniques as data-driven methods can be found in [1, 2]. The classical POD technique, introduced by Lumley [3], remains one of the most popular techniques for capturing coherent structures from flowfield data. One extended version of POD is called Spectral Proper Orthogonal Decomposition (S-POD). In the algorithm, orthogonal modes at discrete frequencies are provided, which are optimally ranked in terms of energy and evolve coherently in both space and time. The details of the mathematical description of this technique can be found in [4].

In this paper, we aim to utilize the S-POD technique to investigate the orthogonal modes in instantaneous and statistical data from a high-speed axisymmetric turbulent jet. We investigate the modal structure of turbulence in high speed jets at two hierarchical levels – the instantaneous flow data obtained directly from a Large-Eddy Simulation (LES) database and its statistics that continues to depend on time through a time shift owing to temporal homogeneity of the unsteady flow. At each level we aim to analyze the degree of modal richness (i.e., energy disparity, spectral uniformity and spectral decay) for both first and second order fluctuating variables and their statistical equivalents (second & fourth order auto-covariances).

2. Spectral Proper Orthogonal Decomposition (S-POD) Theory

In order to compute S-POD modes from discretized flow data, we follow the algorithm presented by [5] and [6]. However, a simplification was applied by [7]. S-POD modes are defined as the eigenvectors of a cross spectral-density tensor at each frequency. The cross-spectral density tensor, which represents correlations between different spatial locations in the difficulty of the S-POD algorithm lies in the spectral computations, where Welch's method is applied

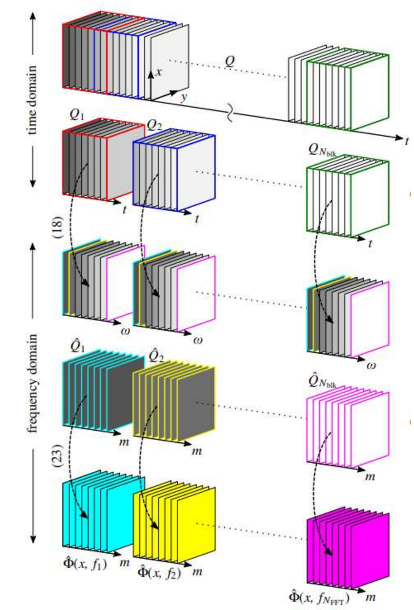

Fig. 1 Schematic of the S-POD algorithm (adapted from [8, 4]

which involves dividing the time series data into overlapping segments and calculating the periodogram for each segment. The theory behind the S-POD algorithm is described in detail in [7, 9]. Here, we briefly explain the algorithm utilized for extracting S-POD modes from the time series data. It should be noted that the S-POD algorithm and MATLAB implementation presented by [9] is used throughout this paper[1].

A schematic of the S-POD algorithm is presented in Figure 1. Initially, the time-domain flow data from various snapshots are organized into a data matrix, denoted as Q. This matrix comprises q_k vectors, representing the spatial state of the flow for each of the M snapshots. The matrix is then segmented into multiple blocks to prepare the data for the Fourier transform. Each segment includes a subset of snapshots and overlaps with adjacent segments. The resulting fast Fourier transform matrix consists of columns $\hat{q}_k^n$, where each $\hat{q}_k^n$ corresponds to the nth realization of the Fourier mode at the kth specific frequency.

Corresponding author: M. Z. A. Koshuriyan
E-mail address: zamir.koshuriyan@york.ac.uk

[1] https://github.com/SpectralPOD/spod-matlab

In the next step, at a single frequency, the cross-spectral density tensor are constructed (see Eq (1)).

$$S_{f_k} = \hat{Q}_{f_k} \hat{Q}^*_{fk}. \quad (1)$$

Finally, the eigenvalue and eigenvectoers of the cross-spectral density matrix provides the S-POD modes and modal energies for the discrete frequencies, by solving the following eigenvalue problem,

$$S_{f_k} W \Psi_{f_k} = \Psi_{f_k} \Lambda_{f_k} \quad (2)$$

at each frequency. The approximate S-POD modes are given by the columns of Ψ_{f_k} and are the ranked according to their corresponding eigenvalues given by the diagonal matrix Λ_{f_k}.

2.1 LES Data

The details and validations for S-POD analysis of various flow problems can be found in [10]. In order to compute S-POD modes for the statistical and instantaneous data, we use the LES database, SP07 with Mach number, $M = 0.9$. Advanced acoustic analogies of the type presented in [11] use self-consistent asymptotic analysis to show that only the R_{1212} component enters the peak jet noise observed at low frequencies. Here, $(1, 2)$ refer to velocity fluctuation in the streamwise and radial directions respectively In the present work, however, we compare the S-POD analysis for second and fourth-order auto-covariances components; i.e., R_{11}, R_{12} versus R_{1111}, and R_{1212}. We obtain the unsteady flow/statistical data for the standard test case for aero-acoustic model testing: i.e., an axi-symmetric round jet with acoustic Mach number $M = 0.9$. The time co-ordinate enters the arguments for R_{ij}/R_{ijkl} via time-delay τ. The spatial co-ordinates η_1 and η_2 represent streamwise/radial components of a separation vector between two spatial field points in the jet ($\boldsymbol{y}$ & $\boldsymbol{y} + \boldsymbol{\eta}$). The location $\boldsymbol{y} = (y_1, r, \psi)$ is fixed at an axial/radial position at the end of potential core ($y_1/D_j = 6.5$) at the jet shear layer ($r/D_j = 0.5$) for the $\psi = 0°$ azimuthal plane. The R_{ij}/R_{ijkl} tensors are defined in the usual way

$$R_{ij}(y, \eta, \tau) = \lim_{T \to \infty} \frac{1}{2T} \int_{-T}^{T} v''_i(y, \tau) v''_j(y+\eta, \tau+\tau_0) d\tau \quad (3)$$

and

$$R_{ijkl}(y, \eta, \tau) = \lim_{T \to \infty} \frac{1}{2T} \int_{-T}^{T} e''_{ij}(y, \tau) e''_{kl}(y+\eta, \tau+\tau_0) d\tau \quad (4)$$

where v''_i is the velocity fluctuation about the Favre-average mean flow [11] and e''_{ij} is the fluctuating Reynolds stress tensor. Figure 2 illustrates the (η_1, η_2) spatial variation of (R_{11}, R_{1111}) at the first time-delay snapshot, τ). Both correlations possess their maxima at this point representing the amplitude of their respective auto-correlations with the fourth order R_{1111} smaller than second order by approximately one order of magnitude.

R_{12}/R_{1212} (Figure 3) behave similarly in terms of the space/time location of the maximum correlation and second versus fourth order correlation.

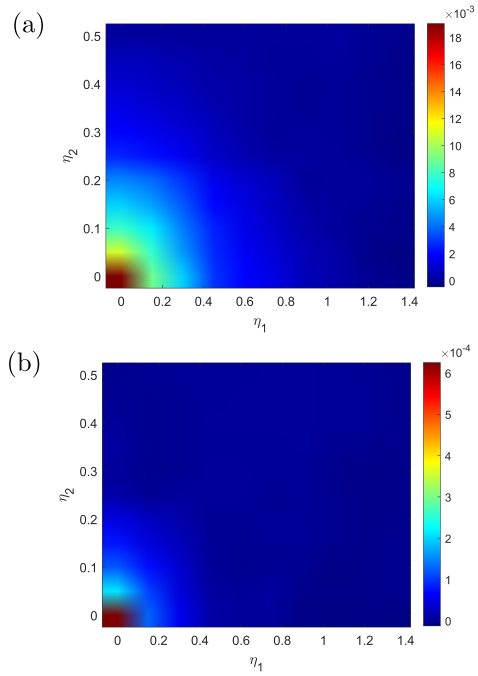

Fig. 2 Correlation function component for the axi-symmetric round jet with $M = 0.9$. a) Second order correlation (R_{11}) for the first snapshot τ, b) Fourth order correlation (R_{1111}) for the first snapshot τ

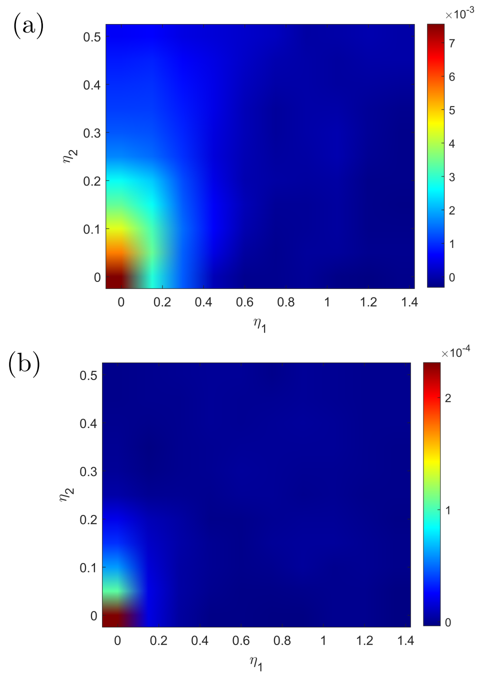

Fig. 3 Correlation function component for the axi-symmetric round jet with $M = 0.9$. a) Second order correlation (R_{12}) for the first snapshot τ, b) Fourth order correlation (R_{1212}) for the first snapshot τ

3. S-POD Analysis and Interpretation

Any three dimensional dataset (two space × time) can be decomposed into a set of statistically orthogonal modes (see summary in §.2). Hence we now construct a graphical representation for the modal energy content of the S-POD modes as a function of frequency. Thus the spatial coordinates are η_1 and

η_2, with time-delay at 51 snapshots. Consequently, we can construct the data matrix as required for the S-POD calculations. This means we obtain the S-POD eigenvalues at each mode k, i.e., $\lambda_k(St)$ where St is the Strouhal number. We refer to the resulting curves as the S-POD eigenvalue spectra. As discussed in Section 2.1, we use a statistical dataset with the variation of the correlation function components of the flow field. Figure 4 indicates the S-POD eigenvalue spectra of the statistical data of an axisymmetric jet described in Section 2.1. Figure 4.a indicates the SPOD eigenvalue spectra of the second order correlation R_{11}, and Figure 4.b represents the S-POD eigenvalue spectra for the fourth order counterpart R_{1111}. In Figure 4, we highlighted first three S-POD modes, shown by solid lines and the others are shown by dashed lines.

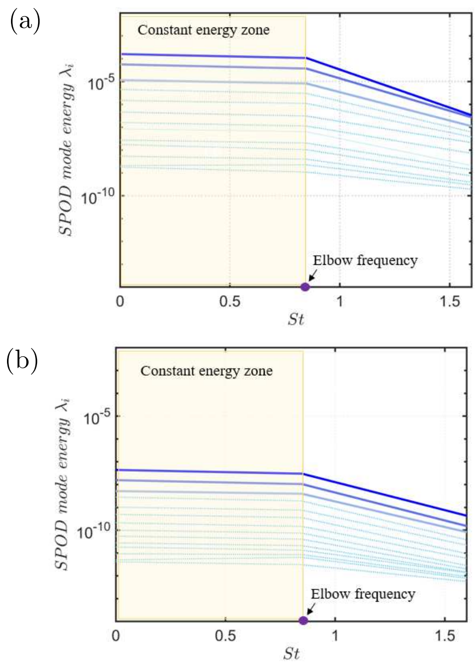

Fig. 4 SPOD mode energy for a) second order correlations R_{11} and b) for fourth order correlation R_{1111} respect to Strouhal number.

The S-POD eigenvalue spectra for both R_{11} and R_{1111} illustrate a relatively constant energy region at low Strouhal numbers. The *spectral elbow* at $St = 0.85$ marks the point of spectral decay where there is a decrease in modal energy. This occurs for both correlations. However, the first and second S-POD modes will reach to the same energy level at the higher frequencies, while the third S-POD modes still exhibit a different energy level. The slope of the first three S-POD modes after the elbow frequency is calculated. The detailed comparison of the properties obtained from the S-POD eigenvalue spectra are shown in Table 1.

As shown in Table 1, for R_{11} the gradient of the first S-POD mode after the elbow frequency decays faster than the second and third S-POD modes. Furthermore, it is evident that as the frequency increases the separation between S-POD modes is smaller (physically representing less energetic modes) and

Table 1 Properties of R_{11} extracted from S-POD eigenvalue spectra.

R11			
	SPOD1	SPOD2	SPOD3
Elbow St	0.85	0.85	0.85
Decay gradient	1.3×10^{-4}	4.3×10^{-5}	3.5×10^{-6}
Max. energy	1.6×10^{-4}	5.6×10^{-5}	1.2×10^{-5}
Max/Min	8.9×10^{4}	3.1×10^{4}	6.4×10^{3}
R1111			
	SPOD1	SPOD2	SPOD3
Elbow St	0.85	0.85	0.85
Decay gradient	3.5×10^{-8}	1.2×10^{-8}	4.6×10^{-9}
Max. energy	4.4×10^{-8}	1.6×10^{-8}	5.2×10^{-9}
Max/Min	1.1×10^{4}	3.9×10^{3}	1.3×10^{3}

the system exhibits low-rank behaviour. Commensurate with the actual amplitude of the auto-covariance components in Fig. 2 and 3, the maximum S-POD energy for the fourth order correlation is smaller than the second order. It is also clear from Table 1 that at higher St, the modal decomposition for R_{1111} does not appear to approach a low-rank (single dominant energy mode) condition. But note that this could be because of the limited temporal snapshots also.

We repeat the S-POD calculations for the R_{12} and R_{1212} shown in Figure 5.a and Figure 5.b respectively. Similarly, we presented the main properties in Table 2. Again, three S-POD modes are highlighted. Similar to Figure 4, the separation between S-POD modes at the lower frequencies are pronounced.

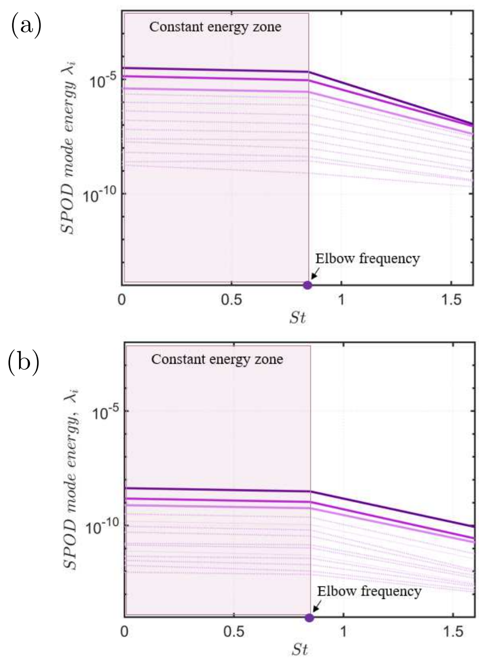

Fig. 5 SPOD mode energy for a) second order correlation R_{12} and b) for fourth order correlation R_{1212} respect to Strouhal number.

4. Concluding Remarks

In this work, we have set out to use the Spectral-Proper Orthogonal Decomposition (S-POD) algorithm to extract the modal energy from a statistical dataset of an axisymmetric, high-speed jet with a Mach number of $M = 0.9$. To achieve this, we

Table 2 Properties of R_{12} and R_{1212} extracted from the S-POD eigenvalue spectra.

R12			
	SPOD1	SPOD2	SPOD3
Elbow St	0.85	0.85	0.85
Decay gradient	2.5×10^{-5}	1.1×10^{-5}	3.3×10^{-6}
Max. energy	1.6×10^{-4}	5.6×10^{-5}	1.2×10^{-5}
Max/Min	1.7×10^{4}	7.8×10^{3}	2.2×10^{3}
R1212			
	SPOD1	SPOD2	SPOD3
Elbow St	0.85	0.85	0.85
Decay gradient	3.9×10^{-9}	1.3×10^{-9}	6.7×10^{-10}
Max. energy	4.3×10^{-9}	1.5×10^{-9}	7.8×10^{-10}
Max/Min	4.7×10^{3}	1.6×10^{3}	8.5×10^{2}

considered both the second and fourth-order correlation function components of the flow data. Various properties related to the energy distribution within the SPOD modes were analyzed. Our findings indicate that, at low Strouhal numbers, the energy contained within these modes remains relatively constant. However, by its nature, the temporal resolution is limited because of the rapid de-correlation at large time delays, which occurs faster at high-order turbulence correlations (R_{ijkl} versus R_{ij}).

Our results, as shown in Figure 4 and 5 , illustrate that the orthogonal mode decomposition reveals a significant disparity between the high and low S-POD eigenvalues. This indicates that the majority of the energy content is concentrated within the first three S-POD modes. The natural next step is to compare statistical to the more traditional use of S-POD, that uses the instantaneous flow field data (i.e. $\boldsymbol{v}''(\boldsymbol{y}, \tau)$ with a resolution of 6000 time files.)

Based on the previous work by [12], where 5000 temporal snapshots were shown to a richer eigen structure for S-POD modes across frequency range. Figure 6 illustrates this comparison. Note that, a reduced number of snapshots with this dataset gives spectral results comparable to the statistical data analysed in the paper. In Figure 6.a, the complete set of 5000 snapshots is used, while Figure 6.b shows the case where the number of snapshots is reduced to 51.

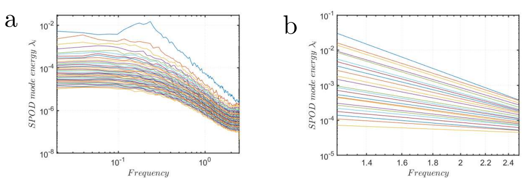

Fig. 6 SPOD mode energy for a jet turbulence presented in [12]. a) full sets of snapshots (5000) b) limited number of snapshots (51).

References

[1] K. Taira, Kunihiko, S. L. Brunton, S. T. M. Dawson,C. W. Rowley, T. Colonius, B. J. McKeon, O. T. Schmidt, S. Gordeyev, V. Theofilis, and L. S. Ukeiley, *AIAA Journal*, 55, (2017), 4013–4041.

[2] C. W. Rowley and S. T. M. Dawson *AIAA Journal*, 49, (2017), 387–417.

[3] J. L. Lumley, *Atmospheric Turbulence and Radio Wave Propagation*, (1967), 166–178.

[4] O. T. Schmidt and T. Colonius, *AIAA Journal*, 58, (2020), 1023–1033.

[5] J. H. Citriniti and W. K. George *Journal of Fluid Mechanics*, 418, (2000), 137–166.

[6] S. V. Gordeyev and F. O. Thomas *Experiments in Fluids*, 54, (2013), 1–16.

[7] A. Towne, O. T. Schmidt and T. Colonius, *Journal of Fluid Mechanics*, 847, (2018), 821–867.

[8] O.T. Schmidt and A. Towne, *Computer Physics Communications*, 237, (2019), 98–109.

[9] O. T. Schmidt and T. Colonius, *AIAA Journal*, 58, (2020), 1023–1033.

[10] O. Es. Sahli, A. Sescu,M. Z. Afsar, O. R. H. Buxton, *Physics of Fluids*, 32, (2020),

[11] M. Z. Afsar, A. Sescu and S. J. Leib, *Philosophical Transactions of the Royal Society A*, 377, (2019), 20190073.

[12] G. A. Brès, P. Jordan, M. Le Rallic, V. Jaunet, A. V. G. Cavalieri, A. Towne, S. K. Lele, T. Colonius, O. T. Schmidt, *J. of Fluid Mech*, 851, (2018), 83–124.